



OPEN

Facile synthesis of spongy NiCo₂O₄ powders for lithium-ion storage

H. Mahboubi, S. M. Masoudpanah[✉], S. Alamolhoda & M. Hasheminasari

Spongy NiCo₂O₄ powders were prepared by solution combustion synthesis (SCS) method for lithium ions storage. The effects of combustion parameters including fuel type (L-lysine, glycine, and urea) and fuel amount on the lithium storage performance of NiCo₂O₄ powders were analyzed by various characterization techniques. Single-phase NiCo₂O₄ powders with extremely porous microstructure showed a strong drop of initial specific capacity up to 350 mAhg⁻¹ which was recovered up to 666 mAhg⁻¹ following 100 charge/discharge cycles. However, the NiCo₂O₄ powders prepared by the urea and L-lysine fuels with the compacted microstructure showed the capacity loss without any recovery. The spongy NiCo₂O₄ powders showed an acceptable capability rate performance (404 mAhg⁻¹ @ 400 mA g⁻¹).

High-energy density lithium-ion batteries (LIBs) are one of the most important choices for electric vehicles (EVs) which are in urgent demand on account of fossil fuel depletion and air pollution^{1,2}. Despite all the advantages of traditional graphite anode, it suffers from low theoretical capacity (372 mAhg⁻¹) and poor safety issues caused by the dendrite formation^{3,4}. Among various anode materials, transition metal oxides (TMOs) such as NiCo₂O₄, MnO₂, Fe₃O₄, CoFe₂O₄, etc. are attracted a great attention as next-generation negative candidates due to the suitable lithiation potential and higher theoretical capacity⁵. The TMOs store electrochemical energy by redox reactions as conversion mechanism due to the absence of vacancy in crystal structure for hosting the Li⁺ ions. The large volume changes of expansion and contraction during the redox reactions lead to the pulverizing and falling off active materials from current collectors, continuously fading capacity via hurting electrical contacts⁶. Previous reports showed that the large volume change limits the application of conversion-type TMOs^{7,8}.

Among various TMOs, nickel cobalt oxide (NiCo₂O₄) with spinel cubic structure has been extensively considered as a promising anode material for LIBs owing to its high theoretical capacity (891 mAhg⁻¹), higher electrical conductivity electrochemical activity than the corresponding monometallic oxides, NiO and Co₃O₄⁹⁻¹¹. Several strategies including compositing with carbon fibers, carbon nanotubes, and graphene/graphene oxide and tuning the morphology have been proposed for improving the cycling performance of NiCo₂O₄ anode¹²⁻¹⁵.

One main goal of this work is to develop a facile, simple, and efficient synthesis method for preparation the porous NiCo₂O₄ material. It is expected that the porous materials show the better cycling performance by tolerating the volume changes during charging/discharging cycles, in addition to facilitating the ions diffusion and easily accessing the electrolyte via pores¹⁶⁻¹⁹.

In this work, the spongy NiCo₂O₄ powders were prepared by solution combustion synthesis (SCS) method which is based on an exothermic reaction between organic fuels and metal nitrates as oxidants¹². A large volume of gases is liberated by burning the organic fuels, leading to the high specific surface areas and large pores^{20,21}. Furthermore, the effects of the amounts and types of organic fuels including glycine, L-lysine, and urea on the structural, microstructural, and electrochemical properties of NiCo₂O₄ powders were explored to clarify the capacity fading mechanism.

Experimental procedures

Synthesis method. Ni(NO₃)₂·6H₂O and Co(NO₃)₂·6H₂O as oxidants and glycine (C₂H₅NO₂), L-lysine (C₆H₁₄N₂O₂), and urea (CO(NH₂)₂) as organic fuels were provided by Merck Co.

Firstly, 1 mmol Ni(NO₃)₂·6H₂O and 2 mmol Co(NO₃)₂·6H₂O and 30 mmol organic fuels were dissolved in 30 mL distilled water. For examining the effects of fuel amounts, the different amounts (molar ratio) of the intended fuel [1.5 (0.5), 3 (1), and 6 (2) mmol] were dissolved in the distilled water. The precursor solutions were homogenized by magnetic stirring. After drying at 90 °C, the gel was combusted on a hot plate by further heating up to 250 °C. The combustion products were then calcined at 450 °C for 1 h with a heating rate of 10 °C min⁻¹ in air atmosphere. For easy presentation, the “G1”, “U1”, and “L1” symbols refer to the NiCo₂O₄ powders obtained by glycine, urea, and L-lysine fuels at a molar ratio of 1, respectively.

School of Metallurgy & Materials Engineering, Iran University of Science and Technology (IUST), Tehran, Iran. ✉email: masoodpanah@iust.ac.ir

Materials characterization. The structural properties were analyzed by an X-ray diffractometer (DRON-8, Bourestnik, Russia) equipped with CuK α radiation ($\lambda = 1.540 \text{ \AA}$). The particle size and shape were examined using a scanning electron microscopy (SEM) (Vega II TESCAN, Czech Republic) at 15 kV. For measuring the N₂ adsorption–desorption isotherms using a BELSORP-mini II, the powders were degassed at 250 °C for 5 h.

Electrochemical characterization. The working electrode was prepared by pasting a slurry of NiCo₂O₄ as active material, polyvinylidene fluoride as binder, and acetylene black as conductive agent (70:15:15 in mass ratio) in N-methyl-2-pyrrolidone on Cu foil. The as-coated foil was then dried at 90 °C in an oven. The mass loading of electroactive material on the Al foil was 1.5–2 mg cm⁻². The electrochemical performance was characterized using CR2016 coin cells assembled in Ar-filled glovebox, with metallic lithium as counter electrode, 1 M LiFP₆ solution (EC:DMC) as electrolyte. The galvanostatic discharge/charge tests were performed in 0.01–3 V vs. Li/Li⁺ on a BTS-5 mV 10 mA battery tester (Neware, China) at different current densities. A Radstat10 system (Kianshar Danesh, Iran) was used to record the electrochemical impedance spectra (EIS) in the frequency range of 0.005–50,000 Hz and cyclic voltammetry in the potential range of 0.01–3.0 V at 0.1 mV s⁻¹. To observe the microstructure of cycled cells, the active materials were extracted from the coated foil by rinsing it with diethylene carbonate (DEC) in the glovebox.

Results and discussion

Figure 1a shows the XRD patterns of the NiCo₂O₄ powders obtained by urea, glycine, and L-lysine fuels. All diffraction peaks are indexed to the cubic spinel structure of NiCo₂O₄ phase with a space group of Fd-3m (PDF#00-073-1702). The absence of any peaks shows the high phase purity of the synthesized NiCo₂O₄ powders. The physicochemical properties of NiCo₂O₄ are strongly dependent on the released heat during the burning of organic fuel which is related to the amount and type of organic fuel. The glycine, urea, and L-lysine molecules with the amino (NH₂) group can release the higher thermal energy, leading to the direct formation of final product. However, the combusted products usually are calcined at higher temperatures to enhance the crystallinity by annihilating the various crystal defects. To evaluate the crystallinity, the dependence of crystallite size and lattice strain on fuel type is presented in Fig. 1b. The U1 powder shows the largest crystallite size of 28 nm, while the G1 and L1 powders have a similar crystallite size of about 11 nm, due to the higher combustion adiabatic temperature by the urea fuel. The released heat and liberated gases determine the combustion adiabatic temperature. Therefore, the lower combustion temperatures by the glycine and L-lysine fuels can be attributed to the higher liberated gaseous products than that of urea fuel during combustion reaction.

Figure 2 compares the SEM images of the G1, U1, and L1 samples. There is a spongy microstructure for the L1 sample (Fig. 2a,d), while the U1 sample (Fig. 2b,e) shows an agglomerated microstructure of spherical particles (~245 nm). The G1 powders are composed of an extremely porous microstructure which the NiCo₂O₄ nanoparticles (79 nm) are aggregated on the pores' wall (Fig. 2c,f). The microstructural features such as porosity, particle size, and specific surface area are mainly dependent on the type and amount of the fuel, determining the combustion rate and combustion temperature. A significant amount of large pores in the G1 powders can be attributed to the fast liberation of gaseous products during the combustion reaction. However, some urea molecules can be hydrolyzed to CO₂ and NH₃, leading to the initial precipitation of hydroxides during gelation process. Therefore, the lower amounts of released gaseous result in the bulky microstructure for the U1 powders by using the urea fuel²².

The 2D distribution of Ni, Co, O, and C elements and EDS spectrum of as-calcined G0.5 powder (Fig. 3) confirm the uniform distribution of Ni and Co elements. Moreover, the atomic ratio of Co/Ni is approximately 1.96 which is in agreement with the theoretical value of 2.

N₂ adsorption/desorption isotherms and pore size distribution plots of the U1 and G1 powders are compared in Fig. 4a and b. The isotherms are IV type with an H3 hysteresis loop, relating to the brittle agglomerations of particles in a foamy microstructure²³. The BET specific surface areas of the U1 and G1 powders are 11 and 20 m² g⁻¹, respectively. Moreover, the BJH plots show that the pores of both samples are mainly smaller than

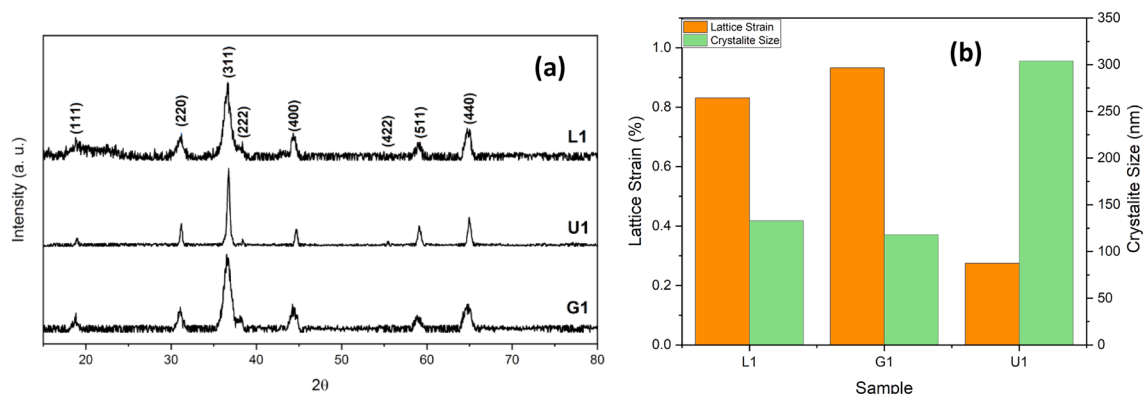


Figure 1. (a) XRD patterns, (b) lattice strain and crystallite size of the as-calcined powders as a function of fuel type.

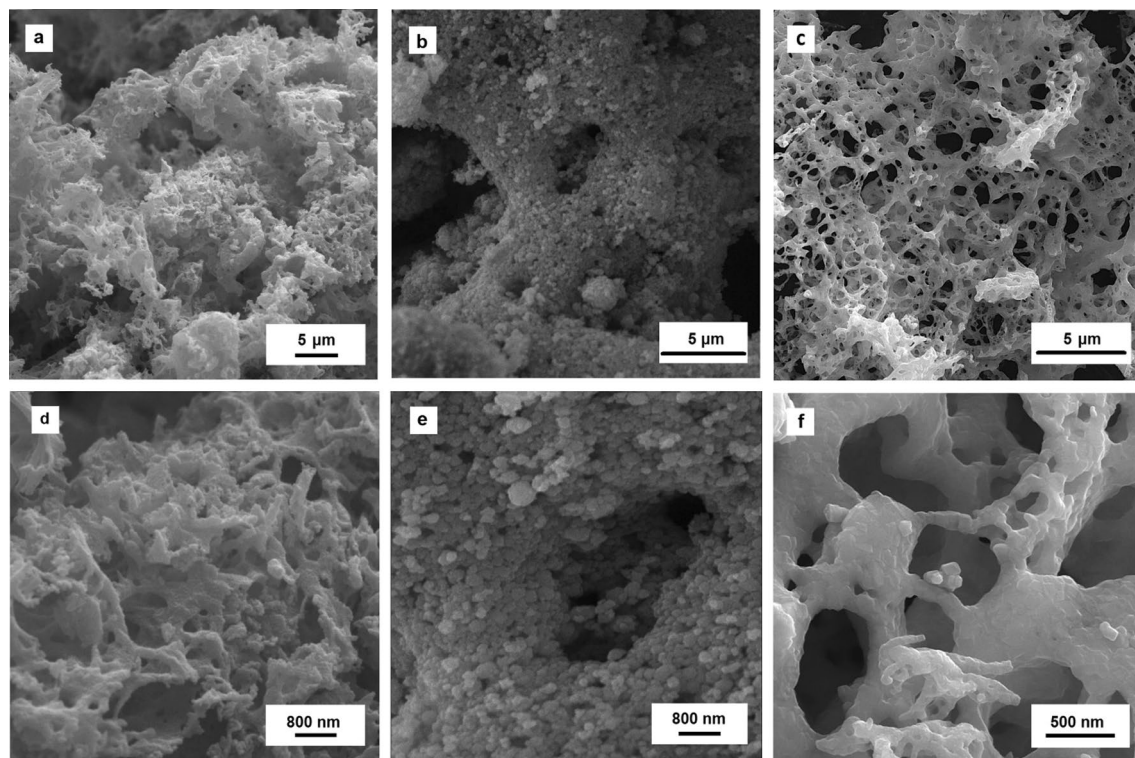


Figure 2. SEM of the as-calcined (a, d) L1, (b, e) U1, (c, f) G1 powders.

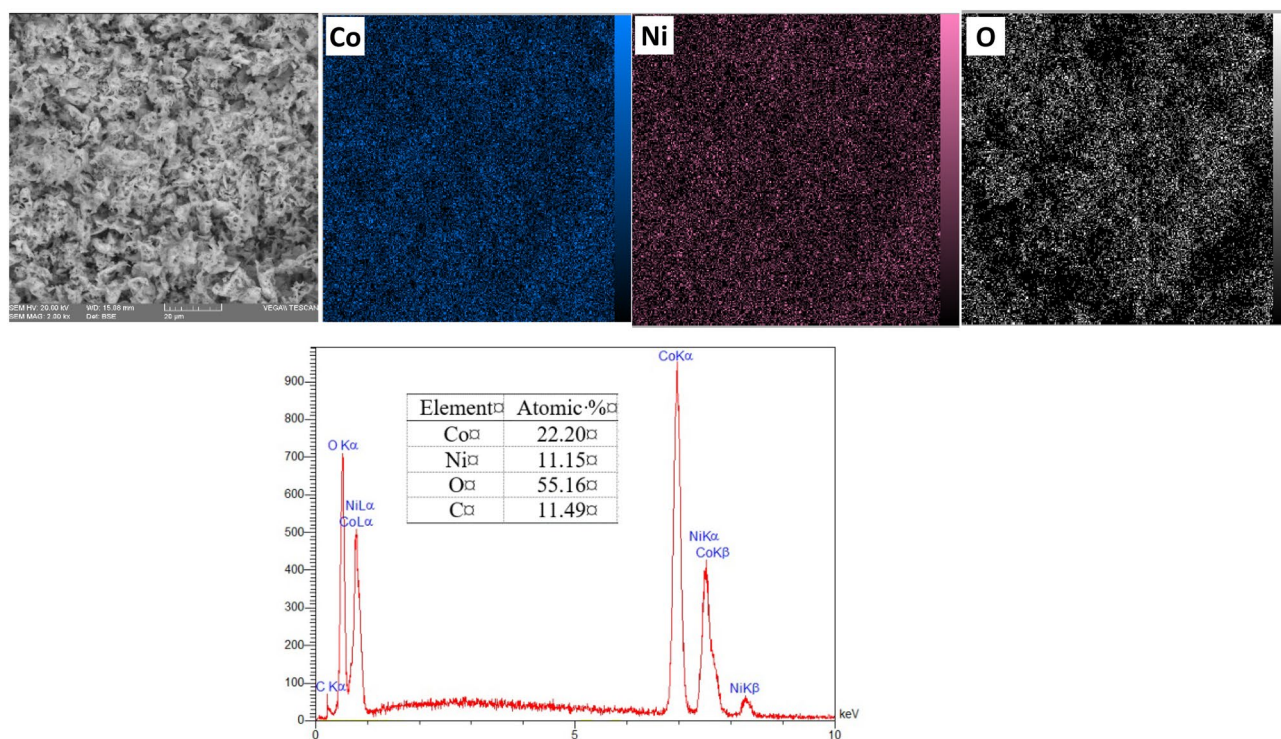


Figure 3. 2D distribution of Ni, Co, and O elements and EDS spectrum in the as-calcined G0.5 powders.

40 nm. The higher combustion temperature leads to a lower specific surface area owing to the particles' growth and sintering. On the other hand, the higher amounts of exhausted gases, the more and the larger pores. Therefore, the higher specific surface areas of the G1 sample is related to the higher amounts of released gaseous products during the combustion reaction²⁴.

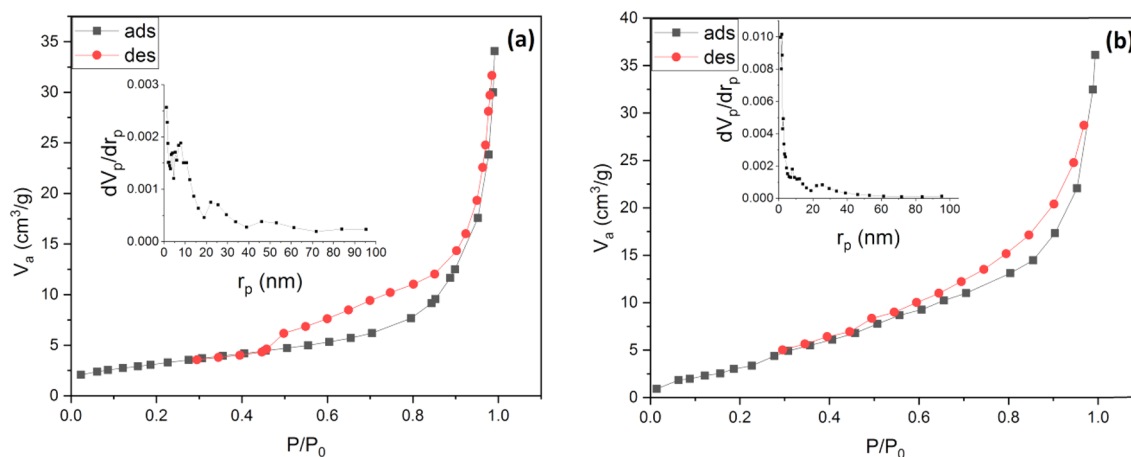


Figure 4. N_2 adsorption–desorption isotherms and pore size plot of (a) U1 and (b) G1 powders.

Figure 5 illustrates the cycling performance of the various powders at a current density of 50 mA g^{-1} in the voltage range of 0.01–3.0 V. Although the G1 sample experiences a capacity fading in the initial cycles, it shows a remarkable improvement during the subsequent cycles. After 100 cycles at 50 mA g^{-1} , the discharge capacity recovered to 664 mAh g^{-1} . However, the cycling performance of the U1 and L1 samples are similar in where the capacity declined and then stabilized at about 200 mAh g^{-1} . Due to the superiority of the cycling performance of the G1 sample, the glycine fuel was selected for further studies. Irrespective of fuel type, the coulombic efficiency is 100%, indicating the high reversibility of charge/discharge processes.

The NiCo_2O_4 powders are also prepared at various molar ratios of glycine fuel to total metal precursor which their XRD patterns are compared in Fig. 6a. All diffraction peaks of the G1 and G0.5 samples are related to the cubic spinel structure of NiCo_2O_4 phase without other impurities. However, there is an impurity NiO phase (PDF2#96-432-0500) together with the NiCo_2O_4 phase, as marked in the diffraction pattern of the G2 powder. The appearance of NiO phase can be attributed to the development of a reducing atmosphere at higher fuel contents which is caused by the higher consumption of O_2 gas. Figure 6b–g show SEM images of the G0.5, G1, and G2 samples. Although the samples synthesized by glycine fuel exhibit a porous microstructure at all fuel contents, but the particle size of NiCo_2O_4 and porosity characteristics are significantly dependent on the fuel contents. The average particle size increased from 18.3 to 78.6 nm for the G0.5 to G1 samples due to the higher combustion temperatures at higher fuel contents. In spite of the larger amounts of liberated gaseous product, the G2 powders have a less porous microstructure because of the premature sintering and subsequent growth of particles²². The cycling performance of the G0.5, G1, and G2 samples is compared in Fig. 6h. The cycling behavior of G0.5 is similar to that of G1 in which a gradual decline occurs at the start, followed by an increase at the end of 100 cycles. The final capacity of the G0.5 samples stands at 535 mAh g^{-1} , which is lower than that of G1 (664 mAh g^{-1}). Furthermore, the capacity fading of the G0.5 powders occurs at greater cycling numbers compared to the G1 electrode. However, the capacity of the G2 electrode continues to decrease and eventually stabilize at 130 mAh g^{-1} . Unlike G0.5 and G1, the cyclic performance of the G2 electrode does not show any significant upward trend, maybe due to the inhomogeneous distribution of NiO impurity²⁵. Figure 6i shows the capability rate performance of the G0.5 and G1 electrodes. The specific capacity of the G1 sample is 672, and 541 mAh g^{-1} at current density of 50, and 200 mA g^{-1} , respectively, returning to 669 mAh g^{-1} when the current density is reduced back to 50 mA g^{-1} . The G0.5 sample shows the same trend by demonstrating specific capacity of 526, and 431 mAh g^{-1} at current density of 50, and 200 mA g^{-1} . The specific capacity of this samples increases to 570 mAh g^{-1} when the current density is returned to 50 mA g^{-1} . Therefore, the G0.5 and G1 samples with the large

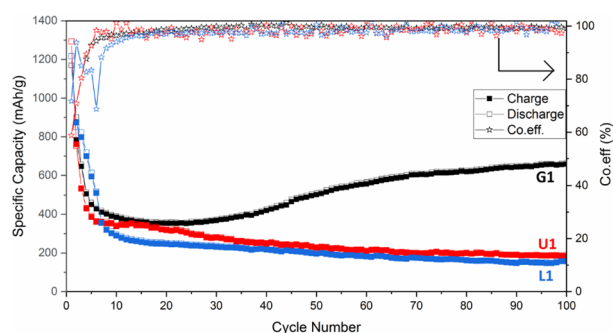


Figure 5. Cycling performance and coulombic efficiency of the L1, U1, and G1 powders.

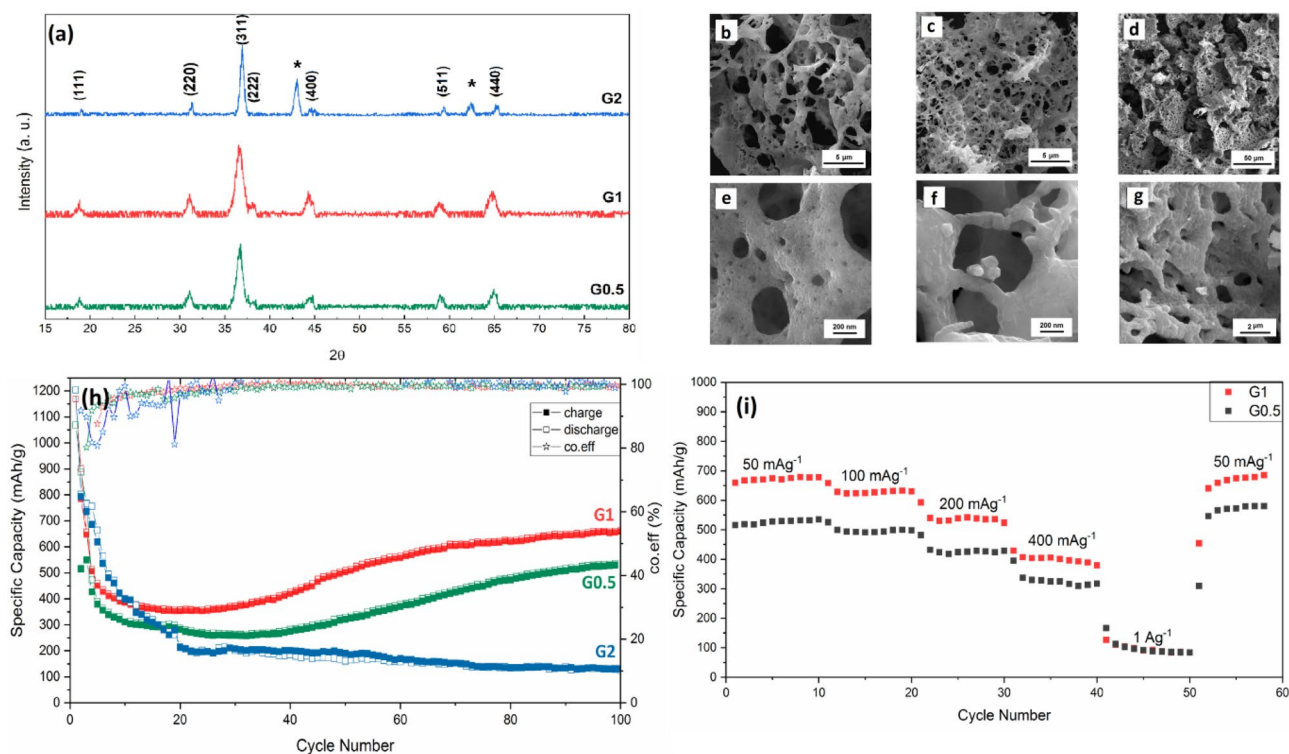
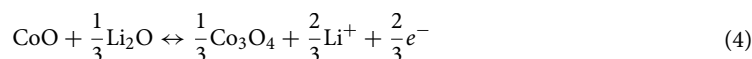
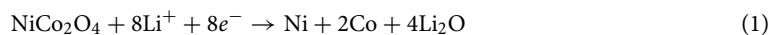


Figure 6. (a) XRD patterns and SEM images of (b, e) G0.5, (c, f) G1, and (d, g) G2 powders and (h) cycling performance and (i) capability rate.

pores and high specific surface area show a high rate capability and cycling performance. Table 1 summarizes the electrochemical performance with previously reported works. The electrochemical properties of the G1 sample are comparable with the NiCo_2O_4 powders synthesized by solvo/hydrothermal methods. However, the spongy G1 material is prepared by facile, simple, and efficient combustion method.

To take a closer look at cycling performance of the G1 sample, the electrochemical performance and microstructural evolution are studied at various cycling numbers. Figure 7a presents the 1st, 2nd, and 3rd CV curves in the voltage range of 0–3.0 V vs. Li/Li^+ and at a scan rate of 0.1 mV s^{-1} . According to the previous reports, the lithiation/delithiation reactions for the NiCo_2O_4 electrode can be presented as follows^{31,32}:



The strong cathodic peak at about 0.75 V vs. Li/Li^+ in the 1st scan can be attributed to the formation of the SEI compounds and metallic Co and Ni at the electroactive material's surface [Eq. (1)]. Because of the irreversible

Morphology	Final discharge specific capacity	Capacity fading (%)	Ref.
Hierarchical micro-nano hydrangea-like	863 mAhg^{-1} @ 100 mA g^{-1} for 100 cycles	47	11
Microellipsoids	820 mAhg^{-1} @ 100 mA g^{-1} for 100 cycles	27	26
Porous Nanorods	650 mAhg^{-1} @ 100 mA g^{-1} for 150 cycles	52	27
Hierarchical nanowire arrays	415 mAhg^{-1} @ 100 mA g^{-1} for 50 cycles	79	28
Bundles of long shaped particles	400 mAhg^{-1} @ 60 mA g^{-1} for 40 cycles	67	29
Hierarchical porous flowers	939 mAhg^{-1} @ 100 mA g^{-1} for 60 cycles	38	30
Spongy powders	666 mAhg^{-1} @ 100 mA g^{-1} for 100 cycles	43	G1 (This work)

Table 1. Comparison of NiCo_2O_4 material with various morphologies.

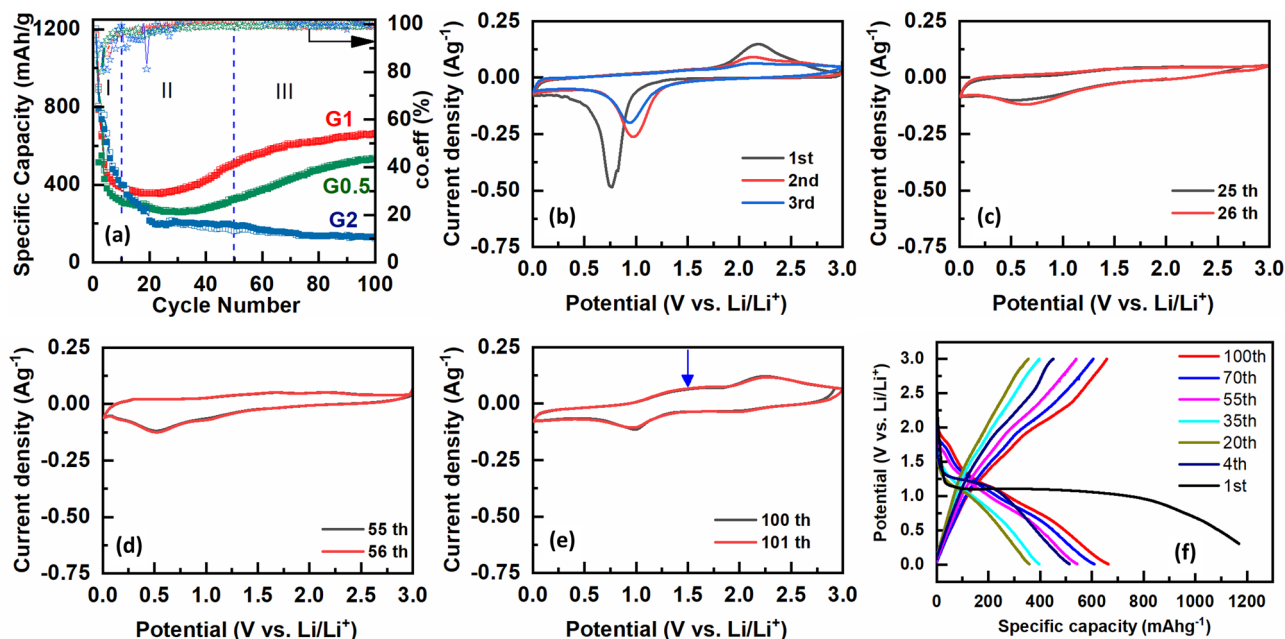


Figure 7. (a) cycling performance of and coulombic coefficient, (b–e) CV curves and (f) charge/discharge profiles of the G1 electrode at various cycles.

reactions that took place at the initial cycle, the reduction peak is shifted and weakened to a higher potential (1 V vs. Li/Li^+) at 2nd and 3rd scans^{30,33}. The oxidation peak at about 2.2 V vs. Li/Li^+ upon lithium extraction process is related to the oxidation peak of Co^0 to Co^{3+} . The oxidation peaks are broadened and weakened by continuous cycling³⁴. The cyclic voltammetry curves don't overlap very well from the second cycle onwards because of the poor reversibility of the electrochemical reactions during the initial charging and discharging cycles. For 25 and 26th cycle, the anodic peaks are broadened, weakened, and hardly detectable in Fig. 7b. However, there is a specific cathodic peak which is slightly intensified by cycling. The anodic and cathodic peaks appear together with the increase of specific capacity as the cycling number reaches to 55th (Fig. 7c). The anodic peak at 1.5 V vs. Li/Li^+ is related to the oxidation of Ni^0 to Ni^{2+} during lithium extraction process³⁵. Furthermore, the redox peaks are intensified upon reaching the 100th cycle (Fig. 7d). The cyclic voltammetry curves approximately overlap by cycling, showing the improvement of reversibility redox reactions.

As previously reported in the literature³⁶, upon the first lithiation/delithiation process, the Li ions are inserted into and extracted from the NiCo_2O_4 material structure, leading to the regional structural collapses by the conversion reaction. The deep lithiation results in the agglomerations and heterogeneous reactions, especially in the large, polycrystalline, porous NiCo_2O_4 particles. The polarization and the structural changes of electroactive materials are responsible for the dramatic capacity loss according to the progressive broadening and severe decay of redox peaks. In other words, the fading of electrochemical reversibility can be attributed to the irreversible formation of some metallic Co and Ni species that continues to accrete the electrode during subsequent cycling³⁵. However, the appearance of $\text{Ni}^0/\text{Ni}^{2+}$ redox peaks is associated with significantly reduced particle size, as will be shown by SEM, immensely improving the lithium-ion diffusion kinetics by providing more sites for lithium-ion storage via increasing the surface area³⁷.

The galvanostatic charge/discharge profiles of the G1 electrode are also shown for their 1st, 2nd, 3rd, 15th, and 100th cycles in Fig. 7. The initial discharge capacity of 1198 mAhg^{-1} decreased up to 508 mAhg^{-1} which can be attributed to the irreversible formation of the SEI and metallic Co and Ni layers. The initial discharge voltage plateau at 1.1 V is related to the conversion mechanism of NiCo_2O_4 , including SEI and metallic Co and Ni formation³⁵. The plateau profile changes to a steeper slope after the 35th discharge cycle which the discharge capacity is reduced to 404 mAhg^{-1} , owing to the structural and textural modifications during the progressive electrochemical cycling³⁸. The plateau profile has transformed into a long potential slope for both the charge and discharge plateau upon the 100th cycle which is related to the increase of discharge and charge capacity up to 658 and 664 mAhg^{-1} , respectively.

The electrochemical impedance spectra (EIS) of the G1 powders after 4, 25, 55, and 100th cycles are given in Fig. 8a to study the interfacial charge-transfer and Li^+ diffusion processes. The Nyquist plots ($-Z''$ vs. Z') include two partially overlapped semicircles and an inclined straight line in the high, medium, and low frequency regions, respectively³⁹. The ohmic resistance of the electrolyte (R_s) is represented by Z_0 intercept at the high-frequency region. The semicircle in the high-frequency range is associated with the solid-electrolyte interface resistance (R_{sf}), while the interface charge transfer resistance (R_{ct}) can be calculated according to the medium-frequency semicircle. The Warburg impedance as inclined line in the low-frequency region is related to the solid state diffusion of Li^+ ions into the electroactive structure³⁹. The values of R_s , R_{sf} , R_{ct} versus cycle number are summarized in Fig. 8b. At initial cycles, the R_{sf} (133 Ω) and R_{ct} (150 Ω) are relatively small. With cycling, up to the minimum specific capacity (25th cycle), the R_{sf} and R_{ct} increase to 673 Ω and 325 Ω , respectively. Interestingly, the value

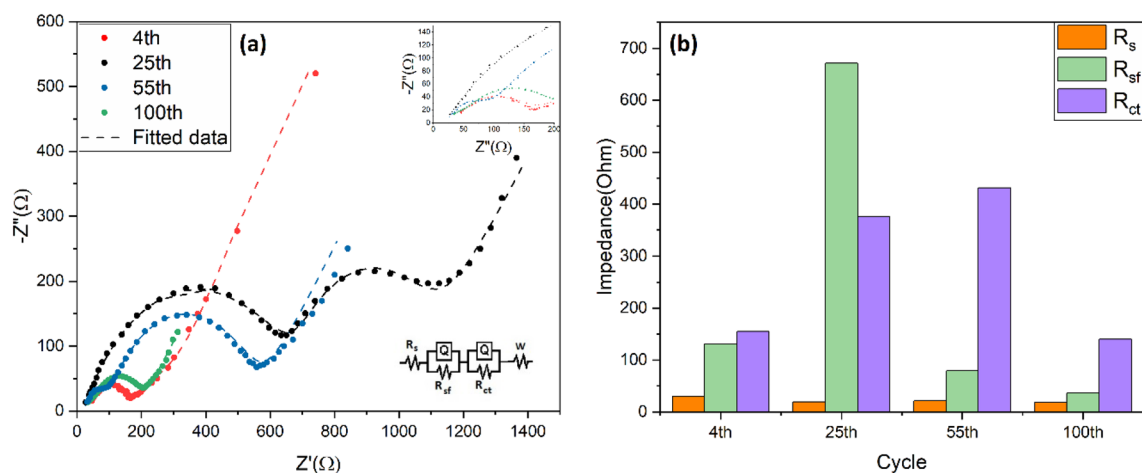


Figure 8. (a) Nyquist plots and the fitted values of the G1 electrode after different cycles, and (b) The values of R_s , R_{sf} , and R_{ct} vs. cycle number.

of R_{sf} is reduced to 71 Ω at 55th cycle as the specific capacity is recovered. The occurrence of these two opposite trends can be attributed to the microstructural evolution of the electrode material⁴⁰. Figure 9 shows the highly porous structure of G1 powders (Fig. 9a,e) was destroyed during the first four cycles, giving way to an agglomerated microstructure (Fig. 9b,f). By cycling, the particles become smaller with a high surface-to-volume ratio, leading to the higher formation of SEI layer⁴¹ which is well consistent with the large R_{sf} at 25th cycle. However, the clusters of nanoparticles are joined together to form coarse clusters at the higher cycle numbers of 55th (Fig. 9c,g) and 100th (Fig. 9d,h), resulting in the lower surface-to-volume ratio and then lower R_{sf} value.

Finally, Stage I (Fig. 7a) is mainly distinguished by the strong drop of specific capacity caused by the initial reactions with the electrolyte and build-up of the SEI and metallic layer^{35,38}. Simultaneously, the phase transitions during electrochemical oxidization of Co^0 and Ni^0 to CoO and NiO result in the pulverization of NiCo_2O_4 particles with initial contact losses between NiCo_2O_4 particles and black carbon as conductive agent. For stage II (Fig. 7a), the coulombic efficiency increases and stabilize up to 100% which is mainly attributed to slow and continuous penetration of the electrolyte through the inner parts of the porous network, gradually penetrating the electrode as well as re-establishment of the contact between pulverized NiCo_2O_4 particles (Fig. 9c,g). The three-dimensional network of porosity between NiCo_2O_4 particles enhance the cycling stability by accommodating volume expansion stresses⁴². The gradual enhancement of capacity in stage III can be ascribed to the consecutive formation and decomposition of a gel-like film containing Li_2O - and some other lithium compounds, facilitating

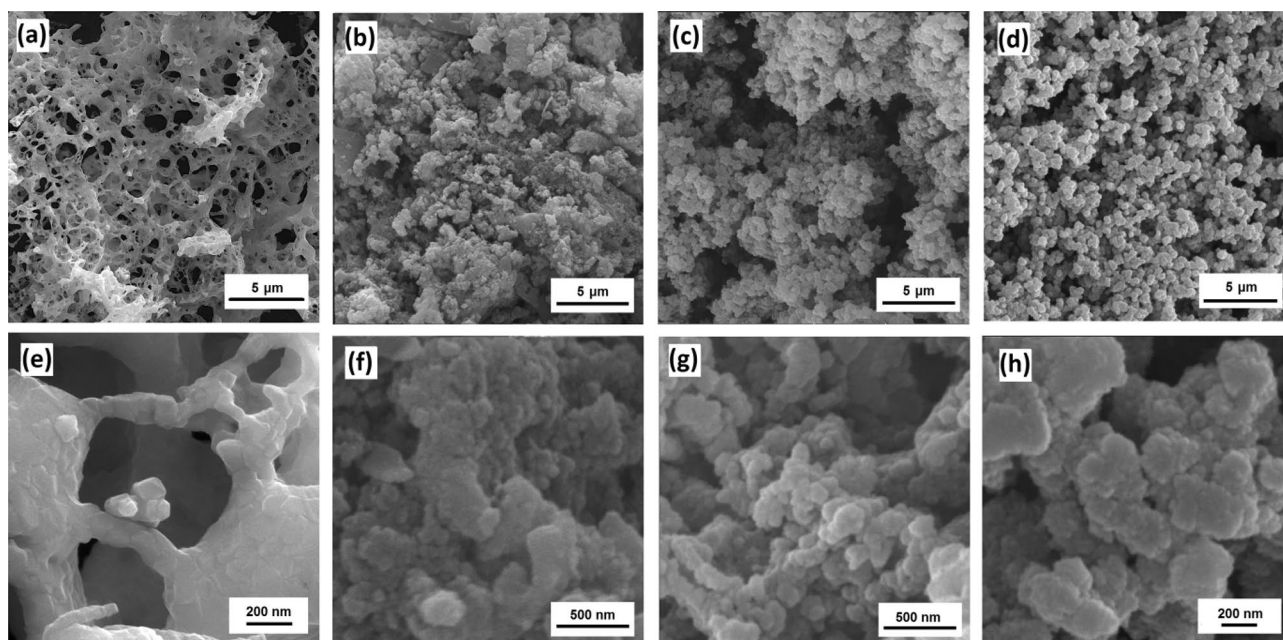


Figure 9. SEM images of the G1 electrode before cycling (a, e) and after 4th (b, f), 25th (c, g), and 100th cycle (d, h).

the transportation of lithium ions. It was reported that the metallic particles are dispersed within the gel-like film, thereby preventing their agglomeration^{43,44}.

Conclusion

The single phase NiCo₂O₄ powders were successfully synthesized by solution combustion method using L-lysine, glycine, and urea as organic fuel. The NiCo₂O₄ powders prepared by glycine and L-lysine fuel showed the porous microstructure owing to the fast liberation of large amounts of gas products. However, the urea fuel led to the agglomerated NiCo₂O₄ nanoparticles on account of the intermediate precipitation of hydroxides during gelation process. A capacity recovery behavior was observed in the porous NiCo₂O₄ powders, while the behavior was previously reported for the transition metal oxide–carbon composite powders. The capacity recovery behavior of the porous NiCo₂O₄ powders was rationalized by various electrochemical tests.

Received: 6 May 2023; Accepted: 20 June 2023

Published online: 23 June 2023

References

- Goodenough, J. B. & Park, K. S. The Li-ion rechargeable battery: A perspective. *J. Am. Chem. Soc.* **135**, 1167–1176 (2013).
- Yi, X. *et al.* Quasi-solid aqueous electrolytes for low-cost sustainable alkali-metal batteries. *Adv. Mater.* **10**, 2302280 (2023).
- Sharova, V., Moretti, A., Giffin, G. A., Carvalho, D. V. & Passerini, S. Evaluation of carbon-coated graphite as a negative electrode material for Li-ion batteries. *Adv. Mater.* **3**, 22 (2017).
- Yang, Y. *et al.* A review on FeOx-based materials for advanced lithium-ion batteries. *Renew. Sustain. Energy Rev.* **127**, 109884 (2020).
- Cai, Z.-L. *et al.* High-pseudocapacitance of porous and square NiO@NC nanosheets for high-performance lithium-ion batteries. *Rare Metal* **40**, 1451–1458 (2021).
- Lu, Z. *et al.* Battery-type Ni-Co-Se hollow microspheres cathode materials enabled by bifunctional N-doped carbon quantum dots with ultrafast electrochemical kinetics for hybrid supercapacitors. *Chem. Eng. J.* **450**, 138347 (2022).
- Zhang, Y. *et al.* Enhanced pseudo-capacitive contributions to high-performance sodium storage in TiO₂/C nanofibers via double effects of sulfur modification. *Nano-Micro Lett.* **12**, 165 (2020).
- Yun, X. *et al.* Heterostructured NiSe₂/CoSe₂ hollow microspheres as battery-type cathode for hybrid supercapacitors: Electrochemical kinetics and energy storage mechanism. *Chem. Eng. J.* **426**, 131328 (2021).
- Kulkarni, P. *et al.* Facile high yield synthesis of MgCo₂O₄ and investigation of its role as anode material for lithium ion batteries. *Ceram. Int.* **45**, 14775–14782 (2019).
- Wei, D. *et al.* A critical electrochemical performance descriptor of ferrites as anode materials for Li-ion batteries: Inversion degree. *Ceram. Int.* **45**, 24538–24544 (2019).
- Zhang, J. *et al.* Hierarchical micro-nano hydrangea-like NiCo₂O₄/V₂O₅ free-standing anode for high-performance lithium-ion batteries. *J. Alloy. Compd.* **938**, 168556 (2023).
- Han, X., Gui, X., Yi, T.-F., Li, Y. & Yue, C. Recent progress of NiCo₂O₄-based anodes for high-performance lithium-ion batteries. *Curr. Opin. Solid State Mater. Sci.* **22**, 109–126 (2018).
- Guan, H.-B. *et al.* Hierarchical microspheres constructed by NiCo₂O₄/NiO@C composite nanorods for lithium-ion batteries with enhanced reversible capacity and cycle performance. *J. Alloy. Compd.* **916**, 165456 (2022).
- Sun, L. *et al.* Controlled synthesis and lithium storage performance of NiCo₂O₄/PPy composite materials. *J. Phys. Chem. Solids* **148**, 109761 (2021).
- Sun, P. P. *et al.* Application of NiO-modified NiCo₂O₄ hollow spheres for high performance lithium ion batteries and supercapacitors. *J. Alloys Compd.* **832**, 154956 (2020).
- Shobana, M. K. & Kim, Y. Improved electrode materials for Li-ion batteries using microscale and sub-micrometer scale porous materials: A review. *J. Alloy. Compd.* **729**, 463–474 (2017).
- Wang, L. *et al.* Porous flower-like ZnCo₂O₄ and ZnCo₂O₄@C composite: A facile controllable synthesis and enhanced electrochemical performance. *Ionics* **26**, 4479–4487 (2020).
- Liu, J. *et al.* Combustion synthesized macroporous structure MFe₂O₄ (M = Zn, Co) as anode materials with excellent electrochemical performance for lithium ion batteries. *J. Alloy. Compd.* **699**, 401–407 (2017).
- Feng, Y., Rao, A. M., Zhou, J. & Lu, B. Selective potassium deposition enables dendrite-resistant anodes for ultrastable potassium-metal batteries. *Adv. Mater.* **12**, 2300886 (2023).
- Varma, A., Mukasyan, A. S., Rogachev, A. S. & Manukyan, K. V. Solution combustion synthesis of nanoscale materials. *Chem. Rev.* **116**, 14493–14586 (2016).
- Karami, M., Masoudpanah, S. M. & Rezaie, H. R. Solution combustion synthesis of hierarchical porous LiFePO₄ powders as cathode materials for lithium-ion batteries. *Adv. Powder Technol.* **32**, 1935–1942 (2021).
- Novitskaya, E., Kelly, J. P., Bhaduri, S. & Graeve, O. A. A review of solution combustion synthesis: An analysis of parameters controlling powder characteristics. *Int. Mater. Rev.* **66**, 188–214 (2021).
- Sing, K. S. W. *et al.* Reporting physisorption data for gas/solid systems. *Handb. Heterogen. Catal.* **65**, 1217–1230 (2008).
- Pourgolmohammad, B., Masoudpanah, S. M. & Aboutalebi, M. R. Effects of the fuel type and fuel content on the specific surface area and magnetic properties of solution combusted CoFe₂O₄ nanoparticles. *Ceram. Int.* **43**, 8262–8268 (2017).
- Li, L. *et al.* Electrospun NiCo₂O₄ nanotubes as anodes for Li- and Na-ion batteries. *J. Alloy. Compd.* **777**, 1286–1293 (2019).
- Zheng, H., Xu, S., Li, L., Feng, C. & Wang, S. Synthesis of NiCo₂O₄ microellipsoids as anode material for lithium-ion batteries. *J. Electron. Mater.* **45**, 4966–4972 (2016).
- Ju, Z. *et al.* A facile method for synthesis of porous NiCo₂O₄ nanorods as a high-performance anode material for Li-ion batteries. *Part. Part. Syst. Charact.* **32**, 1012–1019 (2015).
- Chen, G., Yang, J., Tang, J. & Zhou, X. Hierarchical NiCo₂O₄ nanowire arrays on Ni foam as an anode for lithium-ion batteries. *RSC Adv.* **5**, 23067–23072 (2015).
- Darbar, D. *et al.* Studies on spinel cobaltites, MCo₂O₄ (M = Mn, Zn, Fe, Ni and Co) and their functional properties. *Ceram. Int.* **44**, 4630–4639 (2018).
- Li, L. *et al.* The facile synthesis of hierarchical porous flower-like NiCo₂O₄ with superior lithium storage properties. *J. Mater. Chem. A* **1**, 10935–10941 (2013).
- Zhang, C. *et al.* NiCo₂O₄/biomass-derived carbon composites as anode for high-performance lithium ion batteries. *J. Power Sources* **451**, 227761 (2020).
- Wang, M. Tremella-like NiO/NiCo₂O₄ nanocomposites as excellent anodes for cyclable lithium-ion batteries. *J. Cryst. Growth* **589**, 126685 (2022).

33. Chen, C. *et al.* Tunable oxygen-vacancy mediated NiCo₂O₄ microspheres coupled by holey graphene framework with superior lithium-ion storage properties. *Mater. Chem. Phys.* **292**, 126876 (2022).
34. Wang, W. *et al.* A high-capacity NiCo₂O₄@reduced graphene oxide nanocomposite Li-ion battery anode. *J. Alloy. Compd.* **741**, 223–230 (2018).
35. Cao, M. *et al.* Molten salt synthesis of NiCo-NiCo₂O₄@C nanotubes as anode materials for Li-ion batteries. *J. Colloid Interface Sci.* **636**, 518–527 (2023).
36. Wang, Y. *et al.* Facile preparation of monodisperse NiCo₂O₄ porous microcubes as a high capacity anode material for lithium ion batteries. *Inorg. Chem. Front.* **5**, 559–567 (2018).
37. Gyanprakash, M. & Kumar Rastogi, D. C. Investigation of silicon nanoparticle size on specific capacity of Li-ion battery via electrochemical impedance spectroscopy. *J. Electroanal. Chem.* **931**, 117176 (2023).
38. Liang, Z. *et al.* Urchin like inverse spinel manganese doped NiCo₂O₄ microspheres as high performances anode for lithium-ion batteries. *J. Colloid Interface Sci.* **616**, 509–519 (2022).
39. Gaberšček, M. Impedance spectroscopy of battery cells: Theory versus experiment. *Curr. Opin. Electrochem.* **32**, 100917 (2022).
40. He, F., Wu, L., Wei, G., Zhang, H. & Yan, J. Electrical conductivity and ion transfer behavior of NiCo₂O₄ with different micro structures. *Results Phys.* **16**, 102478 (2020).
41. Nara, H. *et al.* Impedance analysis of LiNi_{1/3}Mn_{1/3}Co_{1/3}O₂ cathodes with different secondary-particle size distribution in lithium-ion battery. *Electrochim. Acta* **241**, 323–330 (2017).
42. Chen, H. *et al.* A new spinel high-entropy oxide (Mg_{0.2}Ti_{0.2}Zn_{0.2}Cu_{0.2}Fe_{0.2})₃O₄ with fast reaction kinetics and excellent stability as an anode material for lithium ion batteries. *RSC Adv.* **10**, 9736–9744 (2020).
43. Ren, Q.-Q. *et al.* Enhanced electrochemical performance by size-dependent SEI layer reactivation of NiCo₂O₄ anodes for lithium ion batteries. *Electrochim. Acta* **297**, 1011–1017 (2019).
44. Kakarla, A. K., Narsimulu, D. & Yu, J. S. Two-dimensional porous NiCo₂O₄ nanostructures for use as advanced high-performance anode material in lithium-ion batteries. *J. Alloy. Compd.* **886**, 161224 (2021).

Author contributions

H.M.: Data curation, Formal analysis. S.M.M.: Supervision, Conceptualization, Writing—review & editing. S.A.: Adviosor, Conceptualization, M.H.: Adviosor, Conceptualization.

Competing interests

The authors declare no competing interests.

Additional information

Correspondence and requests for materials should be addressed to S.M.M.

Reprints and permissions information is available at www.nature.com/reprints.

Publisher's note Springer Nature remains neutral with regard to jurisdictional claims in published maps and institutional affiliations.



Open Access This article is licensed under a Creative Commons Attribution 4.0 International License, which permits use, sharing, adaptation, distribution and reproduction in any medium or format, as long as you give appropriate credit to the original author(s) and the source, provide a link to the Creative Commons licence, and indicate if changes were made. The images or other third party material in this article are included in the article's Creative Commons licence, unless indicated otherwise in a credit line to the material. If material is not included in the article's Creative Commons licence and your intended use is not permitted by statutory regulation or exceeds the permitted use, you will need to obtain permission directly from the copyright holder. To view a copy of this licence, visit <http://creativecommons.org/licenses/by/4.0/>.

© The Author(s) 2023